Double-perovskites A_2FeMoO$_{6-\delta}$ (A = Ca, Sr, Ba) as anodes for solid oxide fuel cells

Leilei Zhang [a], Qingjun Zhou [a,b], Qiang He [a], Tianmin He [a,*]

[a] State Key Laboratory of Superhard Materials, and College of Physics, Jilin University, 2519 Jiefang Road, Changchun 130012, PR China
[b] College of Science, Civil Aviation University of China, Tianjin 300300, PR China

ARTICLE INFO

ABSTRACT

Double-perovskites A_2FeMoO$_{6-\delta}$ (A = Ca, Sr, Ba) have been investigated as potential anode materials for solid oxide fuel cells (SOFCs). At room temperature, A_2FeMoO$_{6-\delta}$ compounds crystallize in monoclinic, tetragonal, and cubic structures for A = Ca, Sr, and Ba, respectively. A weak peak observed at around 880 cm^{-1} in the Raman spectra can be attributed to traces of AMoO$_4$. XPS has confirmed the coexistence of Fe^{2+}–Mo^{6+} and Fe^{3+}–Mo^{5+} electronic configurations. Moreover, a systematic shift from Fe$^{2+/3+}$–Mo$^{6+/5+}$ to Fe^{2+}–Mo^{6+} configuration is seen with increasing A-site cation size. A_2FeMoO$_{6-\delta}$ samples display distinct electrical properties in H$_2$, which can be attributed to different degrees of degeneracy of the Fe^{2+}–Mo^{6+} and Fe^{3+}–Mo^{5+} configurations. Ca$_2$FeMoO$_{6-\delta}$ is unstable in a nitrogen atmosphere, while Sr$_2$FeMoO$_{6-\delta}$ and Ba$_2$FeMoO$_{6-\delta}$ are stable up to 1200 °C. The thermal expansion coefficients of Sr$_2$FeMoO$_{6-\delta}$ and Ba$_2$FeMoO$_{6-\delta}$ are very close to that of La$_{0.9}$Sr$_{0.1}$Ga$_{0.8}$Mg$_{0.2}$O$_{3-\delta}$ (LSGM). The performances of cells with 300 μm thick LSGM electrolyte, double-perovskite SmBaCo$_2$O$_{5+x}$ cathodes, and A_2FeMoO$_{6-\delta}$ anodes follow the sequence Ca$_2$FeMoO$_{6-\delta}$ < Ba$_2$FeMoO$_{6-\delta}$ < Sr$_2$FeMoO$_{6-\delta}$. The maximum power densities of a cell with an Sr$_2$FeMoO$_{6-\delta}$ anode reach 831 mW cm^{-2} in dry H$_2$ and 735 mW cm^{-2} in commercial city gas at 850 °C, respectively.

1. Introduction

Solid oxide fuel cells (SOFCs) are very promising electrochemical devices that convert chemical energy directly into electrical energy with high efficiency while causing little pollution. SOFCs operate at high temperatures, which can promote rapid reaction kinetics. Such high-temperature SOFCs allow internal reforming of hydrocarbon fuels or even direct oxidation. Therefore, SOFCs offer an opportunity for utilization of low-cost and more readily available hydrocarbon fuels, such as natural gas or coal gas, which makes them more competitive in comparison with other fuel cell systems [1–4]. The most common SOFC anode material is based on Ni, which shows good electrochemical performance with pure H$_2$ as fuel. However, this anode is readily fouled by carbon deposition and sulfur poisoning when operated on natural gas [2,3]. In order to overcome this problem, various attempts have been made to develop alternative anode materials that can resist carbon deposition and/or tolerate sulfur contamination when using hydrocarbon fuels [3,5–11]. Among these materials, mixed ionic and electronic conductors have been investigated as potential anode materials, principally chromite- and titanate-based perovskites. For example,

La$_{0.75}$Sr$_{0.25}$Cr$_{0.5}$Mn$_{0.5}$O$_{3-\delta}$, which exhibits high performance when operating in pure H$_2$ and CH$_4$ at high temperatures, is a promising SOFC anode material [4]. However, it shows low electronic conductivity in a reducing atmosphere and low stability in fuels containing 10% H$_2$S [12].

Recently, Huang et al. [13,14] reported that the B-site ordered double-perovskite Sr$_2$MgMoO$_{6-\delta}$ has high resistance to carbon deposition and excellent tolerance to sulfur in natural gas. It showed excellent SOFC anode performance and stability with a variety of fuels. Marrero-Lopez et al. [15] and Bernuy-Lopez et al. [16] further confirmed that this material displayed high redox stability at up to 1000 °C under 5% H$_2$/N$_2$ and 1200 °C under 5% H$_2$/Ar reducing conditions, respectively. More recently, Huang et al. [17] reported other members of the Sr$_2$$MMoO_6$ series as anode materials containing a 3d-block transition metal M (M = Co, Ni). Their results showed that an Sr$_2$CoMoO$_6$ anode displayed high cell output performance in H$_2$ and wet CH$_4$, while an Sr$_2$NiMoO$_6$ anode displayed notable cell output performance only in dry CH$_4$. In addition, Ji et al. [18,19] reported the performances of La-doped Sr$_2$MgMoO$_{6-\delta}$ and Sr$_2$NiMoO$_{6-\delta}$ as anode materials for SOFCs with La$_{0.9}$Sr$_{0.1}$Ga$_{0.8}$Mg$_{0.2}$O$_{3-\delta}$ (LSGM) electrolyte in natural gas and high-carbon fuel, respectively. Their results indicated that an Sr$_{1.2}$La$_{0.8}$MgMoO$_{6-\delta}$ anode displayed an improved performance for the SOFC operating on moderately desulfurized natural gas at 800 °C as compared to an Sr$_2$MgMoO$_{6-\delta}$ anode, while a better cell

* Corresponding author. Tel.: +86 431 88499039; fax: +86 431 88498000.
E-mail addresses: hly@mail.jlu.edu.cn, hetm@jlu.edu.cn (T. He).

performance was attained with $Sr_2NiMoO_{6-\delta}$ as anode when operating on H_2. All of these results indicate that double-perovskites have great potential for use as anode materials in cells operating on natural gas.

Double-perovskites of the $A_2FeMoO_{6-\delta}$ (A = alkaline-earth metal) family, which can be stable at 1200 °C under a low oxygen partial pressure [20], have attracted our attention due to their good catalytic activity for methane oxidation [21]. The catalytic properties of perovskites are closely related to their electronic conductivity, electron delocalization, metal-like behavior, and the nature, oxidation states, and relative arrangement of the B-site cations [21,22]. From this point of view, half-metallic double-perovskites with a double-exchange conduction mechanism seem to be perfect candidates as anodes exhibiting interesting catalytic properties for hydrocarbon reforming.

In this study, we have systematically explored the valence states, transport properties, phase stabilities, and thermal expansion behavior of double-perovskites of the type $A_2FeMoO_{6-\delta}$ (A = Ca, Sr, Ba). The performances of SOFCs with $A_2FeMoO_{6-\delta}$ as anodes have been assessed in various fuels at temperatures of 700–850 °C.

2. Experimental

2.1. Sample preparation

Polycrystalline samples of $A_2FeMoO_{6-\delta}$ (A = Ca, Sr, Ba) were prepared by solid-state reactions. A cation-stoichiometric mixture of starting powders of $SrCO_3$ (or $CaCO_3$, $BaCO_3$) (99%), Fe_2O_3 (99%), and MoO_3 (99.5%) was first calcined at 900 °C in air for 10 h. The calcined powders were pelletized and finally sintered at 1100 °C in 5% H_2/Ar for 10 h to achieve a single phase. The preparations of the other materials used, namely $SmBaCo_2O_{5+x}$ double-perovskite cathode, $La_{0.9}Sr_{0.1}Ga_{0.8}Mg_{0.2}O_{3-\delta}$ (LSGM), and $Ce_{0.8}Sm_{0.2}O_{1.9}$ (SDC) electrolytes, have been described elsewhere [23,24].

2.2. Characterization

The sintered samples were characterized using an X-ray diffractometer (Rigaku D-Max γA, operated at 12 kW) with an angle step size of 0.02° and a scanning range of 15–85° for phase identification and the assessment of phase purity. The structures of the samples were analyzed by means of a Raman spectrometer (Renishaw inVia) equipped with an argon-ion laser operating at an excitation wavelength of 514.5 nm. A scanning electron microscope (SEM, JEOL JSM-6480LV) was used to inspect the surface morphologies of the samples. The local chemical compositions of the samples were analyzed by means of an energy-dispersive X-ray spectrometer (EDS, EDAX CDU) with EDAX ZAF quantification [25]. Surface analysis of the samples was performed using an X-ray photoelectron spectrometer (XPS) (VG Scientific ESCALAB MK II) with an Al Kα (1486.6 eV) radiation source. The binding energy scale of the XPS spectra was calibrated with the C 1s peak at 284.6 eV with a standard deviation of 0.2 eV. The vacuum level in the ultra-high vacuum chamber during XPS measurement was 1.97×10^{-9} Torr. Detailed scans to identify the species in the samples were obtained with a step size of 0.05 eV s^{-1}.

Electrical resistivities of the samples in H_2 were measured by the van der Pauw method over the temperature range 50–850 °C. Thermogravimetric analysis (TGA) and differential scanning calorimetry (DSC) measurements were performed on a NETZSCH STA 449C simultaneous thermal analyzer in a nitrogen atmosphere with a flow rate of 130 mL min^{-1} from 45 to 1000 °C at a heating rate of 10 °C min^{-1}. Thermal expansion coefficients (TEC) were measured using a dilatometer (NETZSCH DIL 402C) with an Al_2O_3 reference.

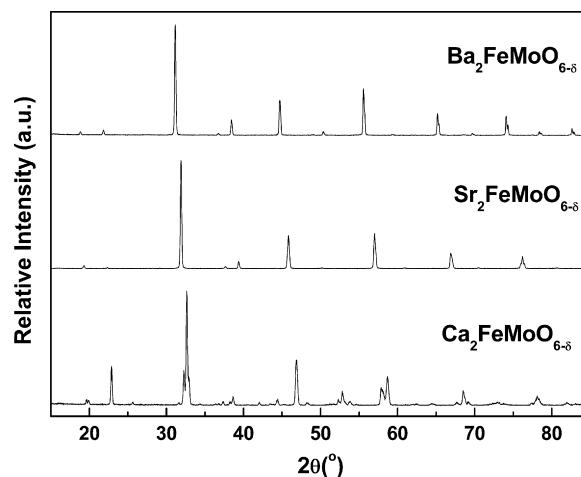**Fig. 1.** XRD patterns of $A_2FeMoO_{6-\delta}$ double-perovskites at room temperature.

The measurements were performed in a nitrogen atmosphere with a flow rate of 60 mL min^{-1}. A heating rate of 5 °C min^{-1} was applied during the measurements.

Single cells were fabricated by an electrolyte-supported technique with 300 μm thick LSGM as the electrolyte, double-perovskite $SmBaCo_2O_{5+x}$ as the cathode, and $A_2FeMoO_{6-\delta}$ as the respective anodes. A thin SDC buffer layer was introduced between the electrolyte and anode to prevent the interdiffusion of ionic species and was fired at 1300 °C for 1 h in air. The anode and the cathode were subsequently fired at 1150 °C for 1 h and 950 °C for 2 h, respectively. During the whole cell fabrication process, both the anode and cathode were fired under a nitrogen atmosphere to prevent re-oxidation and decomposition of the $A_2FeMoO_{6-\delta}$ anodes. The single-cell performances were tested using an electrochemical workstation (CHI604 C). The flow rate of fuel gas (H_2 or city gas) was 100 mL min^{-1}.

3. Results and discussion

3.1. Structural characterization

X-ray diffraction (XRD) patterns of $A_2FeMoO_{6-\delta}$ samples sintered at 1100 °C in 5% H_2/Ar for 10 h are shown in Fig. 1. The $A_2FeMoO_{6-\delta}$ oxides crystallized in a single-phase double-perovskite structure after sintering at 1100 °C. No impurity phases were observed in the XRD patterns of the samples. At room temperature, $Ca_2FeMoO_{6-\delta}$ has a monoclinic structure with space group (s.g.) $P2_1/n$, $Sr_2FeMoO_{6-\delta}$ has a tetragonal structure (s.g. $I4/m$), and $Ba_2FeMoO_{6-\delta}$ crystallizes in a cubic structure (s.g. $Fd-3m$). These results are in good qualitative agreement with those reported by other groups [21,26].

Since $AMoO_4$ impurities could readily be formed during the preparation process of the $A_2FeMoO_{6-\delta}$ [20], the micro-Raman technique was used to detect the appearance of any slight amount of impurity. Fig. 2 shows the Raman spectra of the $A_2FeMoO_{6-\delta}$ samples at room temperature. In the Raman spectrum of $Sr_2FeMoO_{6-\delta}$, besides a weak and broad peak at around 440 cm^{-1}, we observed a broad peak in the frequency range 700–850 cm^{-1}, and a prominent peak at around 880 cm^{-1}. According to the results reported by Son et al. [27], the Raman spectrum of $Sr_2FeMoO_{6-\delta}$ consists of peaks and shoulders at around 770, 620, 440, 390, 290, and 210 cm^{-1}. Therefore, the Raman peak at around 440 cm^{-1} is assigned to the $Sr_2FeMoO_{6-\delta}$ phase. This peak also appears in the Raman spectra of $Ca_2FeMoO_{6-\delta}$ and $Ba_2FeMoO_{6-\delta}$, and can be assigned to the B_g mode [28]. Son et al. [27] also reported that the Raman spectrum of $SrMoO_4$ consists of peaks at
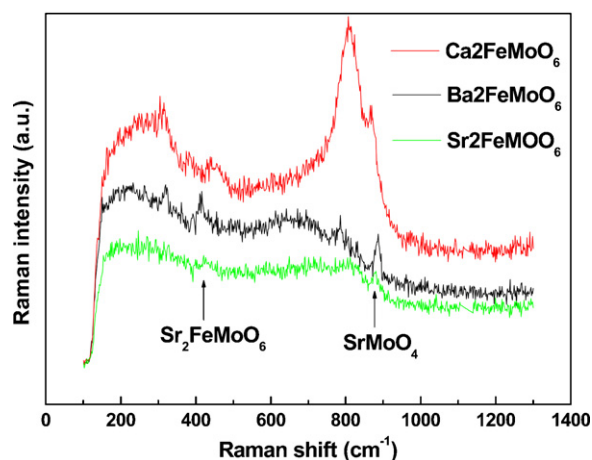
Fig. 2. Raman spectra of $A_2FeMoO_{6-\delta}$ double-perovskites at room temperature.

Fig. 3. SEM micrographs for $A_2FeMoO_{6-\delta}$ double-perovskites sintered at 1100 °C for 10 h in 5 H_2/Ar: (a) $Ca_2FeMoO_{6-\delta}$, (b) $Sr_2FeMoO_{6-\delta}$, and (c) $Ba_2FeMoO_{6-\delta}$.

around 882.3, 840.1, 789, 380, 366, 362, and 179 cm^{-1}. The Raman modes of $SrMoO_4$ in the scheelite-type structure were reported long ago by Porto and Scott [29]. Their results showed that the most intense Raman peak appears at 888 cm^{-1} and corresponds to the stretching A_g vibration of the MoO_4 group. Accordingly, the peak at around 880 cm^{-1} is identified as the signature of the presence of $SrMoO_4$ as an impurity. Similar features are also observed in the Raman spectra of both the $Ca_2FeMoO_{6-\delta}$ and $Ba_2FeMoO_{6-\delta}$ samples, and can be attributed to $CaMoO_4$ and $BaMoO_4$ impurities, respectively. According to the Raman intensity of this mode, the content of $SrMoO_4$ (or $BaMoO_4$) as an impurity in the $Sr_2FeMoO_{6-\delta}$ (or $Ba_2FeMoO_{6-\delta}$) sample was clearly much lower than that of the $CaMoO_4$ impurity in the $Ca_2FeMoO_{6-\delta}$ sample. The XRD results (Fig. 1) showed that the samples obtained were single phases. However, the detection limit of this technique prevents the identification of oxide phases at trace level that may segregate during the preparation process [30]. We could easily detect the presence of the trace $AMoO_4$ impurities by means of Raman spectroscopy.

3.2. SEM and EDS

Fig. 3 shows micrographs of the $A_2FeMoO_{6-\delta}$ samples after sintering at 1100 °C for 10 h in 5% H_2/Ar. All of the samples exhibit a homogeneous distribution of particles. The average grain sizes of the $Ca_2FeMoO_{6-\delta}$, $Sr_2FeMoO_{6-\delta}$, and $Ba_2FeMoO_{6-\delta}$ oxides are about 5–8, 1–2, and 3–4 μm, respectively. The densification of the $Ca_2FeMoO_{6-\delta}$ sample is much higher than that of the $Sr_2FeMoO_{6-\delta}$ and $Ba_2FeMoO_{6-\delta}$ samples. To examine the local chemical homogeneity and to determine the elemental compositions of the oxides, EDS microanalysis was performed on different surface regions for each sample. The EDS spectra of the $A_2FeMoO_{6-\delta}$ samples indicated
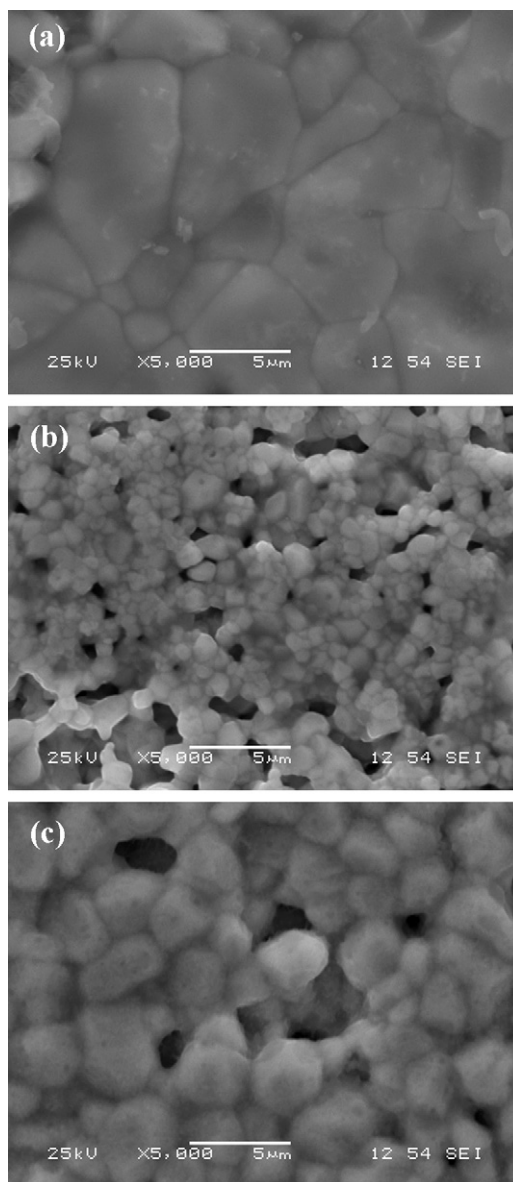
only the constituent elements of Sr (or Ca, Ba), Fe, Mo, and O. Three to four parallel EDS microanalysis measurements were carried out, and the average atomic concentration for each element is shown in Table 1. As can be seen from Table 1, the experimental values are in good agreement with the nominal ones, showing that we obtained

Table 1
Nominal and experimental stoichiometric index of $A_2FeMoO_{6-\delta}$ double-perovskites.

Samples	Element		
	Ca/Sr/Ba	Fe	Mo
$Ca_2FeMoO_{6-\delta}$			
Nominal stoichiometric index	2	1	1
Experimental stoichiometric index	1.954 ± 0.004	0.913 ± 0.008	1.133 ± 0.009
$Sr_2FeMoO_{6-\delta}$			
Nominal stoichiometric index	2	1	1
Experimental stoichiometric index	2.12 ± 0.01	0.961 ± 0.001	0.915 ± 0.008
$Ba_2FeMoO_{6-\delta}$			
Nominal stoichiometric index	2	1	1
Experimental stoichiometric index	2.06 ± 0.01	0.969 ± 0.001	0.97 ± 0.01

Fig. 4. O 1s core-level spectra of $A_2FeMoO_{6-\delta}$ double-perovskites at room temperature.

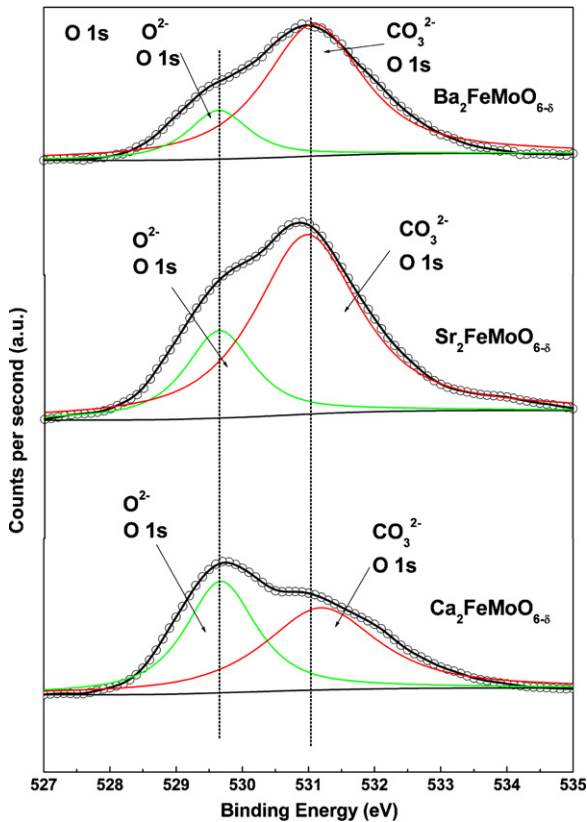**Fig. 5.** Fe 2p core-level spectra of $A_2FeMoO_{6-\delta}$ double-perovskites at room temperature.

Fig. 6. Mo 3d core-level spectra of $A_2FeMoO_{6-\delta}$ double-perovskites at room temperature.

stoichiometric index $A_2FeMoO_{6-\delta}$ oxides. This result is in very good agreement with the XRD measurements.

3.3. XPS analysis

XPS was used to assess the surface properties of the $A_2FeMoO_{6-\delta}$ samples and the chemical environments of Ca (or Sr, Ba), Fe, Mo, and O, which were estimated by curve-fitting of the O 1s, Fe 2p, Mo 3d, and Ca 2p (or Sr 3d, Ba 3d) spectra. The XPS spectra of these species are shown in Figs. 4–7. The binding energies and the percentage contributions of the valence states are shown in Table 2. It can be seen from Fig. 4 that the O 1s core-level spectra consist of two components at around 531.0 and 529.6 eV. The former comes from lattice O^{2-} (O_L) and the latter is typical of hydroxyl groups and carbonate structures (O_H) [21,31]. The O_L/O_H atomic ratios for the $Ca_2FeMoO_{6-\delta}$, $Sr_2FeMoO_{6-\delta}$, and $Ba_2FeMoO_{6-\delta}$ samples were estimated as 1.22, 0.32, and 0.23, respectively. This result indicates that the proportion of carbonate (O_H) compared to O_L increases with increasing size of the A-site cation. The reason for this phenomenon is that the alkaline-earth metal species are segregated towards the surface to form carbonates [21,32]. The XRD results did not reveal the presence of a carbonate component, thus the effect caused by carbonates is negligible.

Fig. 5 shows the Fe 2p core-level spectra of the $A_2FeMoO_{6-\delta}$ samples at room temperature. The Fe 2p XPS of $A_2FeMoO_{6-\delta}$ consists of Fe 2p3/2 and Fe 2p1/2 excitations. Excitation from the Fe 2p3/2 level gives rise to a peak at 710.8 eV (Fe^{3+} 2p3/2), a main peak at 709.1 eV (Fe^{2+} 2p3/2), and a small shoulder at about 706.6 eV (Fe^0 2p3/2). This finding is in good agreement with results reported by Falcón et al. [21]. Fig. 6 shows the Mo 3d core-level spectra of the $A_2FeMoO_{6-\delta}$ samples at room temperature. The Mo 3d XPS spectra show two rather broad peaks at around 232 eV (3d 5/2) and 235 eV (3d 3/2) on the binding energy scale. Curve fitting of the 3d 5/2 spectra yielded
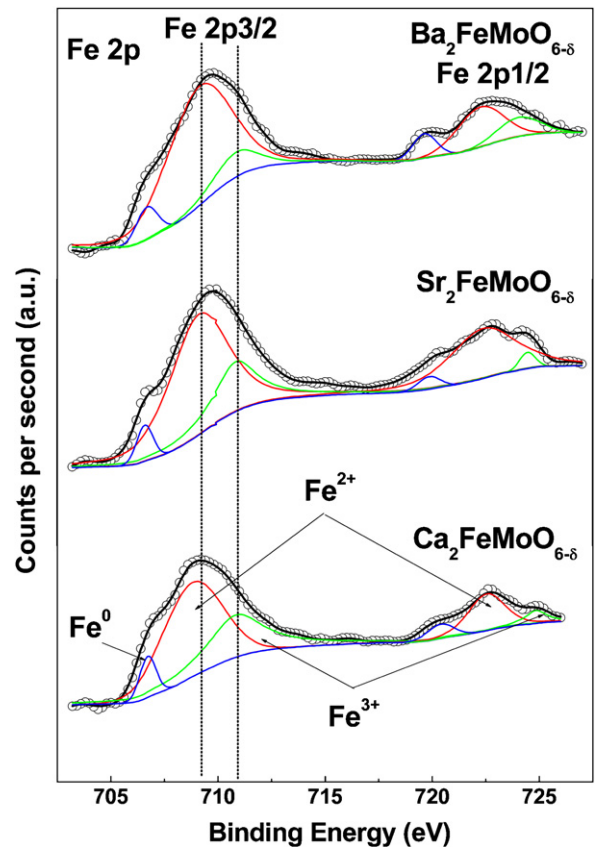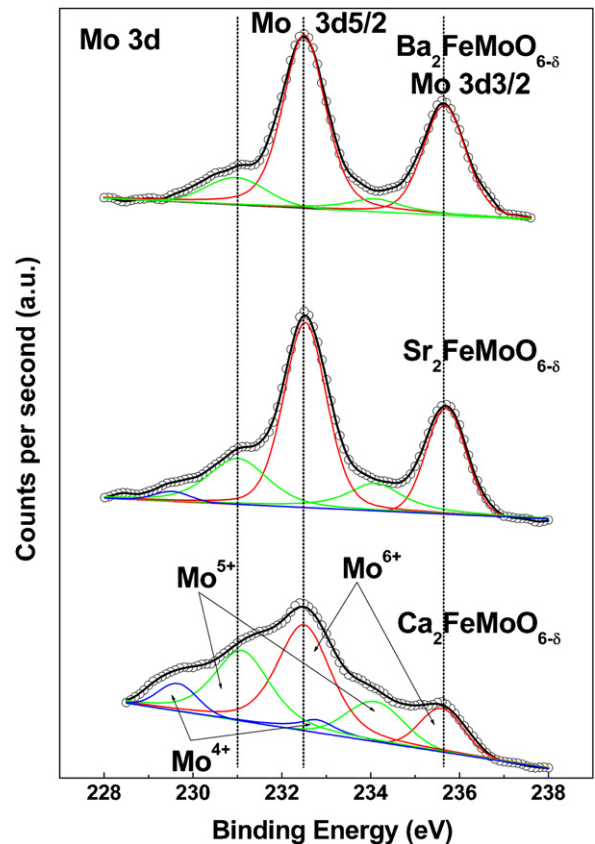
Table 2
Binding energies and percentage contributions of core electrons of $A_2FeMoO_{6-\delta}$ double-perovskites. The percentage contributions of Fe^0 and Mo^{4+} were neglected for their small amounts.

Sample	O 1s		Fe 2p$_{3/2}$			Mo 3d$_{5/2}$			Ca 2p$_{3/2}$ Sr 3d$_{5/2}$ Ba 3d$_{5/2}$
	O_L	O_H	Fe^{3+} (%)	Fe^{2+} (%)	Fe^0	Mo^{5+} (%)	Mo^{6+} (%)	Mo^{4+}	
$Ca_2FeMoO_{6-\delta}$	529.68	531.20	710.81 (40.1%)	708.80 (59.9%)	706.73	231.10 (41.9%)	232.50 (58.1%)	229.66	346.43
$Sr_2FeMoO_{6-\delta}$	529.65	530.97	710.83 (27.4%)	710.83 (72.6%)	706.59	231.00 (27.6%)	232.52 (72.4%)	229.52	133.13
$Ba_2FeMoO_{6-\delta}$	529.64	531.20	710.84 (14.3%)	710.84 (85.7%)	706.67	230.97 (14.3%)	232.51 (85.7%)	–	780.20
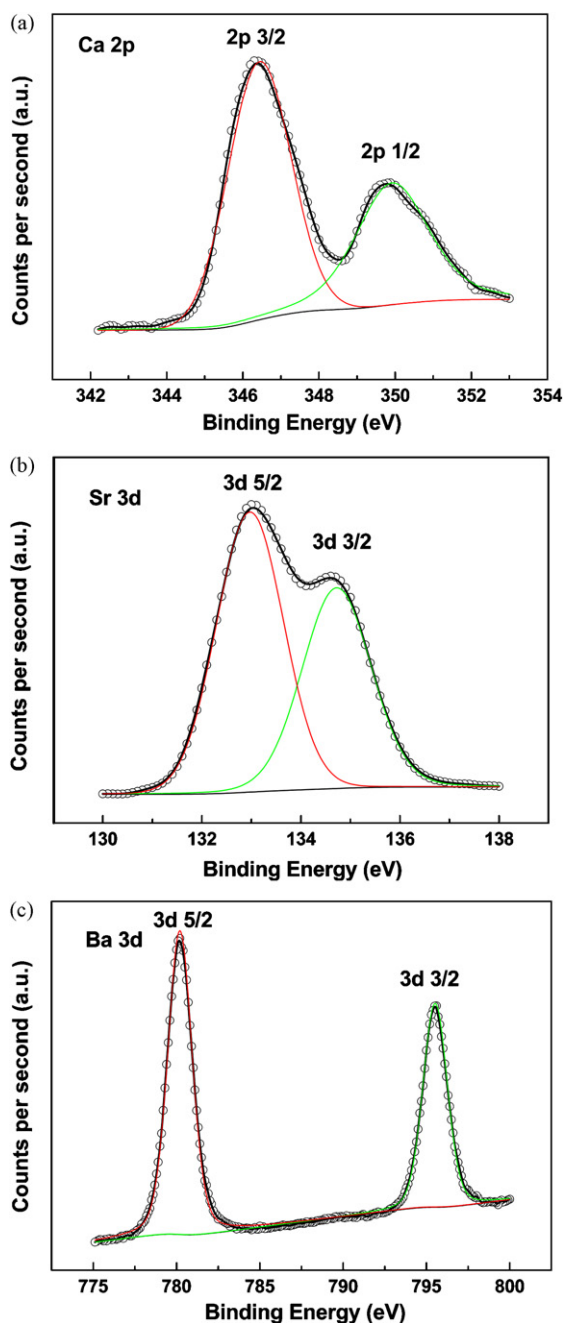
Fig. 7. Ca 2p, Sr 3d, and Ba 3d core-level spectra of $A_2FeMoO_{6-\delta}$ double-perovskites at room temperature.

three components at around 232.5 eV (Mo^{6+} 3d 5/2), 231.1 eV (Mo^{5+} 3d 5/2), and 229.6 eV (Mo^{4+} 3d 5/2) (except in the case of the $Ba_2FeMoO_{6-\delta}$ sample). The small fitted peak of the $Ca_2FeMoO_{6-\delta}$ (or $Sr_2FeMoO_{6-\delta}$) sample at around 229.6 eV can be attributed to surface defect states because: (i) the Fe 2p3/2 spectra also show a weak shoulder on the low binding energy side, and (ii) similar effects of surface defects have been seen for other transition metal components [33–35]. No parasitic phases of Fe^0 and Mo^{4+} species were detected in the samples by either XRD or Raman observations. Therefore, although trace quantities may be present, the amounts of Fe^0 and Mo^{4+} species are negligible. As can be seen in Table 2, the contributions of the Fe^{2+}–Mo^{6+} and Fe^{3+}–Mo^{5+} configurations are quite different among the $Ca_2FeMoO_{6-\delta}$ to $Ba_2FeMoO_{6-\delta}$ samples. The mixed-valence state involves around 27.4% Fe^{3+} ($3d^5$; $S = 5/2$)–Mo^{5+} ($4d^1$; $S = 1/2$) and 72.6% Fe^{2+} ($3d^6$; $S = 2$)–Mo^{6+} ($4d^0$; $S = 0$) for the $Sr_2FeMoO_{6-\delta}$ sample at room temperature, which is in good agreement with the results reported by Kuepper et al. (30% Fe^{3+}–Mo^{5+} and 70% Fe^{2+}–Mo^{6+} electronic configurations) [35] and by Besse et al. (34% Fe^{3+}–Mo^{5+} and 66% Fe^{2+}–Mo^{6+} electronic configurations) [36]. The results for the $Ca_2FeMoO_{6-\delta}$ and $Ba_2FeMoO_{6-\delta}$ samples are also shown in Table 2. From these results, we can conclude that the valence balance of $Fe^{2+/3+}$–$Mo^{5+/6+}$ gradually shifts closer to that of Fe^{2+}–Mo^{6+} as the A-site cation size is increased, which would promote B-site ordering [37,38].

Fig. 7 shows the Ca 2p, Sr 3d, and Ba 3d core-level spectra of the $A_2FeMoO_{6-\delta}$ double-perovskites. The intense Ca 2p, Sr 3d, and Ba 3d XPS spectra could be satisfactorily fitted to one component, indicating that the contributions to the spectra of the minor carbonate component and the main double-perovskite component could not be separated.

The above detailed XPS analysis should provide further insight into the conduction and catalytic action of $A_2FeMoO_{6-\delta}$. The existence of mixed-valent Mo^{5+}/Mo^{6+} provides electronic conductivity with a sufficiently large work function to accept electrons from H_2 and hydrocarbons in the anodic atmospheres of an SOFC. Meanwhile, the presence of oxygen vacancies in the oxygen lattices of $A_2FeMoO_{6-\delta}$ creates good oxide ion conduction. To use the Mo^{5+}/Mo^{6+} couple as a catalyst in a perovskite, a double-perovskite with an M(II) (3d-block transition metal) partner ion is needed to compensate the charge balance [13], and hence the Fe^{2+}/Fe^{3+} couple is introduced in $A_2FeMoO_{6-\delta}$. Therefore, the mixed-valent Mo^{5+}/Mo^{6+} and Fe^{2+}/Fe^{3+} couples play an important role in the conduction and electrochemical performance of $A_2FeMoO_{6-\delta}$.

3.4. Electrical properties

Fig. 8 shows the bulk electrical resistivities as a function of temperature for the $A_2FeMoO_{6-\delta}$ samples in H_2 between 50 and 850 °C. The electrical resistivity of $Ca_2FeMoO_{6-\delta}$ is indicative of metallic-like conduction behavior throughout the whole measured temperature range. The electrical resistivity of $Sr_2FeMoO_{6-\delta}$, on the other hand, is indicative of various conduction behaviors in three regions: (i) it indicates metallic conduction behavior below 150 °C, (ii) it indicates a semiconducting region or localization of
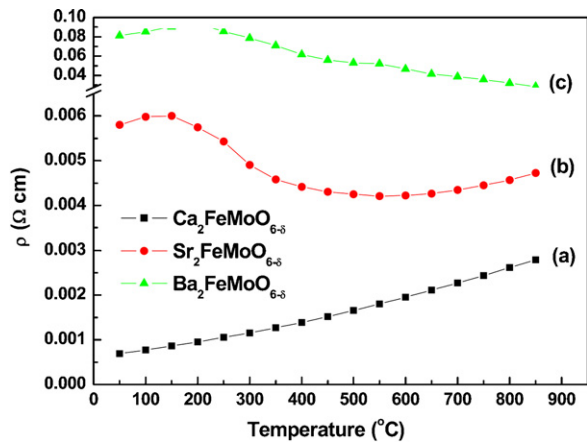
Fig. 8. Bulk electrical resistivities as functions of temperatures of $A_2FeMoO_{6-\delta}$ double-perovskites in H_2: (a) $Ca_2FeMoO_{6-\delta}$, (b) $Sr_2FeMoO_{6-\delta}$, and (c) $Ba_2FeMoO_{6-\delta}$.

the carriers in the temperature range 150–550 °C, and (iii) the sample reverts to metallic conduction behavior between 550 and 850 °C. An insulator–metal transition is found at around 550 °C, which is much higher than that reported in a previous study (at around 317 °C under a vacuum of approximately 10^{-6} Torr) [39]. This difference can be attributed to the different testing conditions. Below 150 °C, the electrical resistivity of $Ba_2FeMoO_{6-\delta}$ is also indicative of metallic conduction behavior. However, the resistivity indicates a semiconducting region or localization of the carriers in the temperature range 200–850 °C. It is noteworthy that the electrical resistivity of $A_2FeMoO_{6-\delta}$ in H_2 over the whole temperature range investigated shows a clear increase by several orders of magnitude in the order: Ca < Sr < Ba. The double-exchange mechanism can be invoked to explain this result (see below).

In $A_2FeMoO_{6-\delta}$, the Fe^{3+} ($3d^5$ $t_{2g}^3 e_g^2$) ions are envisaged as being in a high-spin state with all the spin-up 3d orbitals occupied. Sleight and Weiher [40] proposed that if the spin-down $3d^5$ ($t_{2g}^3 e_g^2$) orbitals of Fe have similar energy to the $4d^1$ (t_{2g}^1) orbitals of Mo, they can form a narrow band and provide the conduction band. This is supported by band-structure calculations, which show a mixing of the spin-down 2p, 3d, and 4d bands of O, Fe, and Mo, respectively, at the Fermi level [41]. In a delocalized Fe^{3+}–Mo^{5+} configuration, the $3d^5$ Fe electrons are localized while the $4d^1$ Mo electrons are itinerant or delocalized. If the $4d^1$ Mo electrons have spin down, the itinerant electrons may be able to hop through the O 2p orbitals to the t_{2g} Fe down empty states, giving rise to a sort of double-exchange mechanism, as proposed by Zener [42] in relation to Fe^{3+}–O–Mo^{5+}–O–Fe^{2+} charge transport. Clearly, the itinerant or delocalized electrons play an important role in the conduction mechanism. With appropriate annealing, $Sr_2FeMoO_{6-\delta}$ samples can be made into insulating, semimetallic, or metallic oxides [41,43], which is quite unusual because the charge ordering of the extreme Fe^{3+}–Mo^{5+} configuration is expected to give rise to exclusively insulating properties. Delocalized Mo electrons or cation nonstoichiometry could explain the metallic behavior of the Sr_2FeMoO_6 material. Sleight and Weiher [40] suggested that the Fe^{3+}–Mo^{5+} configuration could be degenerate with the Fe^{2+}–Mo^{6+} configuration and that this valence degeneracy could be the cause of the observed metallic behavior.

All of the $A_2FeMoO_{6-\delta}$ samples exhibit metallic behavior at low temperatures (Fig. 8), which suggests that the Fe^{2+}–Mo^{6+} configuration may indeed be degenerate with the Fe^{3+}–Mo^{5+} configuration to form a narrow band. This valence degeneracy means that the energy of the π^*–β Mo level is nearly the same as that of the π^*–β level of Fe [40]. With decreasing A-site cation size, the contribution of the Fe^{3+}–Mo^{5+} configuration to the XPS spectrum

increases (15% for Ba, 27% for Sr, and 40% for Ca) (Table 2), while the magnitude of the electrical resistivity decreases (Fig. 8). This suggests that the magnitude of the electrical resistivity is closely related to the degree of degeneracy and hybridization between the Fe^{2+}–Mo^{6+} and Fe^{3+}–Mo^{5+} states. The electrical resistivities of the $Sr_2FeMoO_{6-\delta}$ and $Ba_2FeMoO_{6-\delta}$ samples are indicative of a semiconducting region or localization of the carriers, which may be related to a weak Anderson localization induced by some disorder in the Fe and Mo sites or the presence of oxygen vacancies [39,44]. However, the electrical resistivity of the $Ca_2FeMoO_{6-\delta}$ sample is solely indicative of metallic behavior. This means that the higher the degree of valence degeneracy, the stronger the tendency towards metallic behavior.

3.5. TGA–DSC

To examine the phase stabilities of the $A_2FeMoO_{6-\delta}$ samples, simultaneous TGA–DSC measurements were carried out under a nitrogen atmosphere, and an XRD study was also performed after the thermal analysis. Fig. 9(a) and (b) shows the TGA–DSC curves obtained between 45 and 1000 °C in a nitrogen atmosphere. The TGA curve of $Ca_2FeMoO_{6-\delta}$ differs distinctly from those of $Sr_2FeMoO_{6-\delta}$ and $Ba_2FeMoO_{6-\delta}$, in that the former displays a sharp weight gain, while the latter show only a slight decrease or gain in weight compared to the initial weight. Meanwhile, a sharp endothermic peak is observed at about 426 °C in the DSC curve of $Ca_2FeMoO_{6-\delta}$, but not in the curves of the Sr and Ba analogues. For $Ca_2FeMoO_{6-\delta}$, the weight gain from the initial weight to the weight at 1000 °C is 3.4%, a value that is in good agreement with the theoretical weight gain (~2.8%) for the decomposition of $Ca_2FeMoO_{6-\delta}$

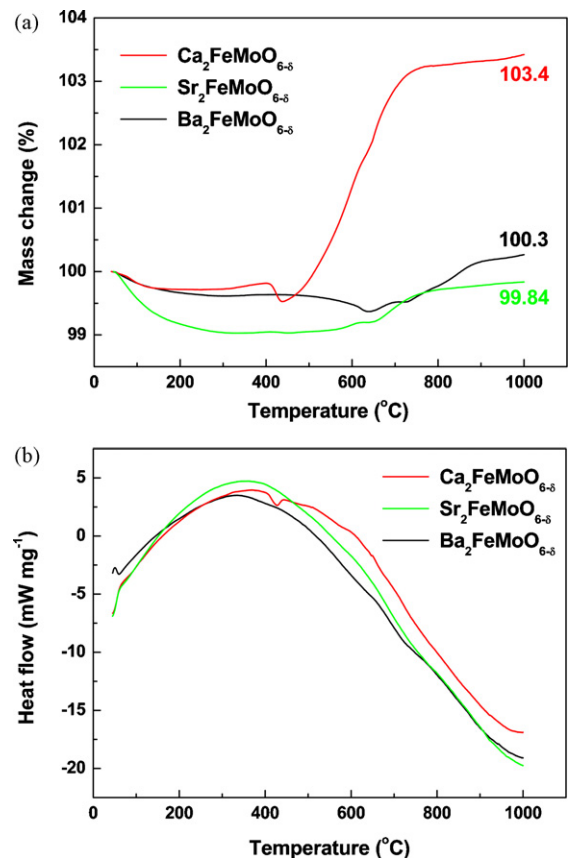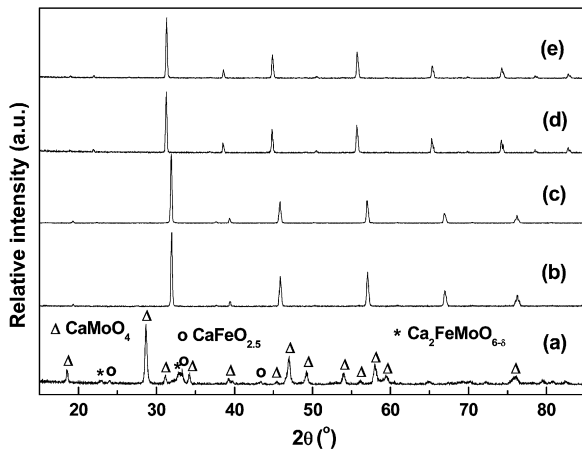**Fig. 9.** (a) TGA and (b) DSC curves of $A_2FeMoO_{6-\delta}$ double-perovskites between 30 and 1000 °C in nitrogen atmosphere.

Fig. 10. XRD patterns of $A_2FeMoO_{6-\delta}$ double-perovskites after TGA–DSC measurements for (a) $Ca_2FeMoO_{6-\delta}$, (b) $Sr_2FeMoO_{6-\delta}$, and (d) $Ba_2FeMoO_{6-\delta}$; XRD patterns of (c) $Sr_2FeMoO_{6-\delta}$ and (e) $Ba_2FeMoO_{6-\delta}$ after sintering at 1200 °C for 2 h in nitrogen atmosphere.

into $CaMoO_4$ and $CaFeO_{2.5}$ according to the following equation [20]:

$$Ca_2FeMoO_{6-\delta} \rightarrow CaMoO_4 + CaFeO_{2.5} \qquad (1)$$
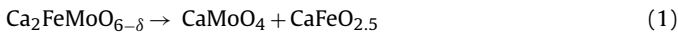
where the oxygen deficiency δ is selected to be 0.04–0.07 based on reports for similar compounds of the type $A_2MgMoO_{6-\delta}$ [16,45,46]. Therefore, the steep weight gain of the sample seen above 430 °C in the TGA curve is due to the decomposition of $Ca_2FeMoO_{6-\delta}$, and is accompanied by an endothermic peak at about 426 °C in the DSC curve. The phase composition of the final products could be indexed by XRD as a mixture of $CaMoO_4$ and $CaFeO_{2.5}$ (Fig. 10), which are in good agreement with the above thermal analysis results.

The weight decreases observed for $Sr_2FeMoO_{6-\delta}$ and $Ba_2FeMoO_{6-\delta}$ in the TGA curves below 650 °C in a nitrogen atmosphere are accompanied by broad exothermic peaks in the DSC curves. This weight loss corresponds to the expulsion of lattice oxygen atoms and the formation of oxygen vacancies in $Sr_2FeMoO_{6-\delta}$ and $Ba_2FeMoO_{6-\delta}$ according to the reaction:

$$2Mo^{\times}_{Mo} + O^{\times}_O \rightarrow 2Mo'_{Mo} + V^{\bullet\bullet}_O + \frac{1}{2}O_2 \uparrow \qquad (2)$$
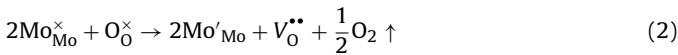
where $O^{\times}_O$ denotes lattice oxygen, $Mo^{\times}_{Mo}$ denotes Mo^{6+}, Mo'_{Mo} denotes Mo^{5+}, and $V^{\bullet\bullet}_O$ is the oxygen vacancy. Similar results have been reported by other groups [17,47,48], even in hydrocarbon and reducing atmospheres. Above 650 °C, the weight increases slightly and the TGA curve levels off; no exothermic peak is seen in the DSC curves. Due to the inevitable presence of a small amount of residual oxygen in the nitrogen atmosphere, the weight gains observed for the $Sr_2FeMoO_{6-\delta}$ and $Ba_2FeMoO_{6-\delta}$ samples above 650 °C can be considered as being due to partial oxidation and oxygen absorption of the sample during the heating run [21]. The final weights at 1000 °C compared to the original weights are 100.3 and 99.8% for $Sr_2FeMoO_{6-\delta}$ and $Ba_2FeMoO_{6-\delta}$, respectively, indicating that these materials are stable in a nitrogen atmosphere. To further confirm the stabilities of the $Sr_2FeMoO_{6-\delta}$ and $Ba_2FeMoO_{6-\delta}$ samples, they were examined by XRD after sintering at 1200 °C for 2 h in a nitrogen atmosphere. As expected, no impurity phases or diffraction peak shifts were observed in the respective XRD patterns (Fig. 10). The XRD results were consistent with the above TGA–DSC analysis.

3.6. Thermal expansion behavior

Thermal expansion compatibility is an indispensable consideration in the development of electrode materials for SOFCs. A

thermal expansion incompatibility between the SOFC components would cause excessive thermal stress, induce delamination of the electrodes during the sintering and operating processes, and hence reduce the lifetime of the SOFCs [49]. Fig. 11(a) shows thermal expansion curves obtained for samples of $A_2FeMoO_{6-\delta}$ and LSGM between 30 and 1000 °C in a nitrogen atmosphere. To identify the volume change of $A_2FeMoO_{6-\delta}$, the TEC curves are shown in Fig. 11(b). The $Sr_2FeMoO_{6-\delta}$ sample has a TEC of 13.9×10^{-6} K^{-1} between 30 and 1000 °C, which is slightly higher than that of the $Ba_2FeMoO_{6-\delta}$ sample (13.3×10^{-6} K^{-1}). Falcón et al. [21] investigated the oxidation profiles of $A_2FeMoO_{6-\delta}$ oxides. Their results showed that oxygen was relatively easily incorporated into the perovskite structure, with the amounts conforming to the sequence: $Ca_2FeMoO_{6-\delta} < Ba_2FeMoO_{6-\delta} < Sr_2FeMoO_{6-\delta}$. This suggests that the concentration of oxygen vacancies also follows the same sequence. In Section 3.5, the TGA curves showed that the number of oxygen vacancies in $Sr_2FeMoO_{6-\delta}$ is higher than those in $Ca_2FeMoO_{6-\delta}$ and $Ba_2FeMoO_{6-\delta}$ (for example, the maximum weight loss was 0.28% for $Ca_2FeMoO_{6-\delta}$, 0.52% for $Ba_2FeMoO_{6-\delta}$, and 0.97% for $Sr_2FeMoO_{6-\delta}$), which agrees well with the above results reported by Falcón et al. [21]. With the increase in the oxygen vacancy concentration, oxygen permeation and lattice expansion become much more pronounced [50]. Therefore, the TEC of $Sr_2FeMoO_{6-\delta}$ is slightly larger than that of $Ba_2FeMoO_{6-\delta}$. It can, however, be noted that a curvature is observed at about 700 °C in the thermal expansion curve for $Ca_2FeMoO_{6-\delta}$, corresponding to a marked decrease in the TEC curve, which may be attributed to the decomposition of $Ca_2FeMoO_{6-\delta}$, as confirmed by the above TGA-DSC and XRD analyses. This indicates that $Ca_2FeMoO_{6-\delta}$ is incompatible as an anode material for application in SOFCs. No abrupt changes were observed in the TEC curves for samples $Sr_2FeMoO_{6-\delta}$ and $Ba_2FeMoO_{6-\delta}$, indicating that there is no structural phase transition in these two oxides in the studied temperature range. The TEC of LSGM electrolyte is 11.2×10^{-6} K^{-1}
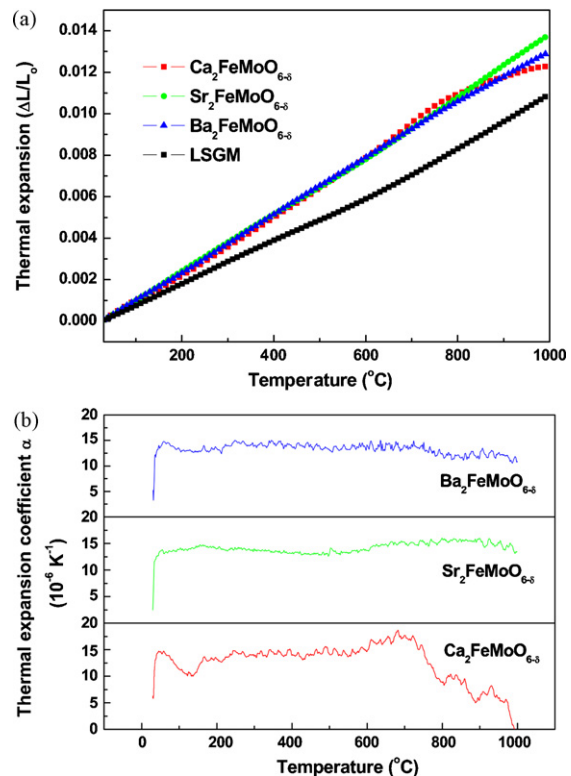
Fig. 11. (a) Thermal expansion and (b) TEC curves of $A_2FeMoO_{6-\delta}$ double-perovskites between 30 and 1000 °C in nitrogen atmosphere.
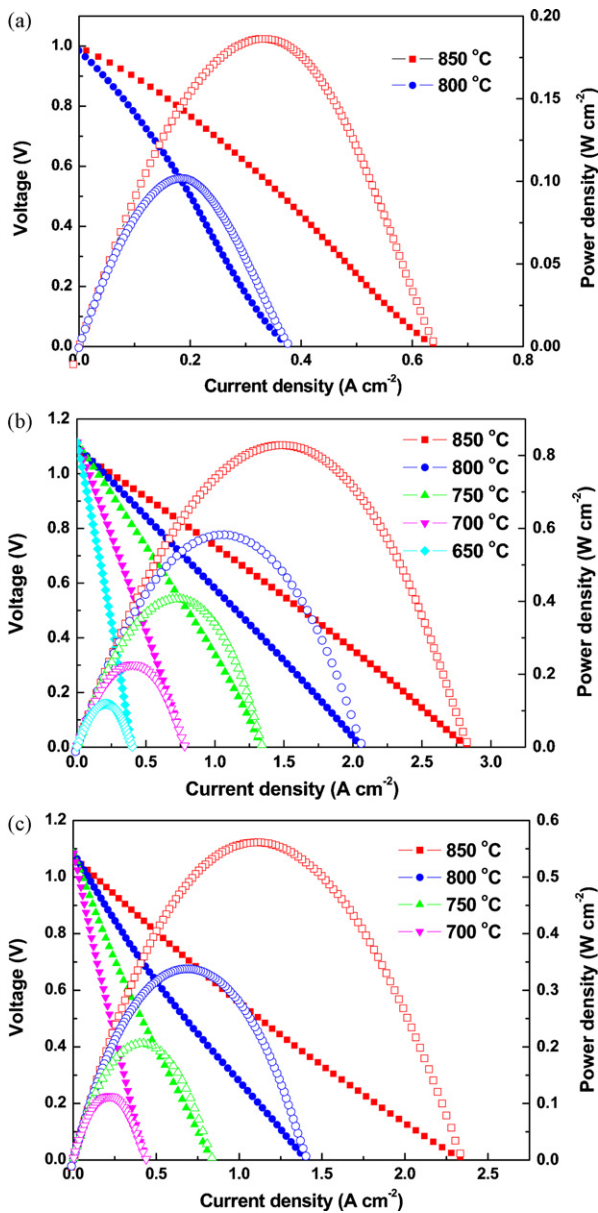
Fig. 12. Power density and cell voltage as functions of current density at different temperatures in H$_2$ for anodes: (a) Sr$_2$FeMoO$_{6-\delta}$, (b) Ba$_2$FeMoO$_{6-\delta}$, and (c) Ca$_2$FeMoO$_{6-\delta}$.

in a nitrogen atmosphere, which is close to the values of the Sr$_2$FeMoO$_{6-\delta}$ and Ba$_2$FeMoO$_{6-\delta}$ samples. Thus, the Sr$_2$FeMoO$_{6-\delta}$ and Ba$_2$FeMoO$_{6-\delta}$ samples show good thermal compatibility with the LSGM electrolyte between 30 and 1000 °C.

3.7. Single-cell electrochemical performance, stability, and SEM

Fig. 12 shows plots of power density and voltage as functions of current density for A_2FeMoO$_{6-\delta}$/SDC/LSGM/SmBaCo$_2$O$_{5+x}$ cells at 700–850 °C using dry H$_2$ as fuel and ambient air as oxidant. The cell with an Sr$_2$FeMoO$_{6-\delta}$ anode exhibited maximum power densities (P_{max}) of 831, 584, and 412 mW cm^{-2} at 850, 800, and 750 °C, respectively, while the cell with a Ba$_2$FeMoO$_{6-\delta}$ anode exhibited P_{max} values of 561, 338, and 206 mW cm^{-2} at these respective temperatures. However, the cell with Ca$_2$FeMoO$_{6-\delta}$ merely achieved a P_{max} of 186 mW cm^{-2} at 850 °C. These results indicate that the cell P_{max} with H$_2$ as fuel for the A_2FeMoO$_{6-\delta}$ anodes increases in the order: Ca$_2$FeMoO$_{6-\delta}$ < Ba$_2$FeMoO$_{6-\delta}$ < Sr$_2$FeMoO$_{6-\delta}$, which

is consistent with the previous report on the catalytic activity of A_2FeMoO$_{6-\delta}$ for methane oxidation [21]. The high catalytic activity of Sr$_2$FeMoO$_{6-\delta}$ is related to the defective character of this double-perovskite, such as its oxygen vacancies [21]. As mentioned in relation to the TGA–DSC data, the number of oxygen vacancies in Sr$_2$FeMoO$_{6-\delta}$ is higher than that in Ba$_2$FeMoO$_{6-\delta}$. Thus, the Sr$_2$FeMoO$_{6-\delta}$ anode displays better electrochemical performance compared to the Ba$_2$FeMoO$_{6-\delta}$ anode. The poor cell performance of the Ca$_2$FeMoO$_{6-\delta}$ anode could be attributed to the decomposition of this material and its smaller number of oxygen vacancies, as corroborated by the above TGA–DSC and XRD analyses.

Fig. 13 shows SEM micrographs of the SOFCs with A_2FeMoO$_{6-\delta}$ as anodes after cell testing. The surfaces of the anodes can be seen to display a homogeneous distribution of particle sizes. The buffer layer can readily be seen between the A_2FeMoO$_{6-\delta}$ anode and LSGM electrolyte, which efficiently prevents interfacial reaction between the anode and electrolyte. The thickness of the SDC layer is about 10 μm. This SDC buffer layer shows good interfacial contacts with the Sr$_2$FeMoO$_{6-\delta}$ and Ba$_2$FeMoO$_{6-\delta}$ anodes. However, the interfacial contact between the Ca$_2$FeMoO$_{6-\delta}$ anode and the SDC buffer layer is inferior to those with the aforementioned two anodes, which may be ascribed to the decomposition of Ca$_2$FeMoO$_{6-\delta}$ that occurs during the cell fabrication process and operation. This further indicates that Ca$_2$FeMoO$_{6-\delta}$ is unsuitable for use as an anode in SOFCs. In addition, it can be seen from Fig. 13 that the anodes have a porous microstructure and moderate porosity, which is favorable for the transfer of fuel gas. The LSGM electrolyte is also dense, although it contains some small closed pores.

To demonstrate the high performance of the Sr$_2$FeMoO$_{6-\delta}$ anode, we present electrochemical impedance spectroscopy data for a single cell operated at different temperatures under open-circuit conditions, as shown in Fig. 14(a). The highest frequency intercept on the real axis represents the ohmic resistance (R_{ohm}) from the electrolyte, the electrodes, the connection wires, and the testing conditions; the lowest frequency intercept represents the total resistance (R_{tot}) of the whole cell. Hence, the distance between the two intercepts corresponds to the interfacial resistance (R_p) [51]. R_p mainly corresponds to the adsorption, diffusion, and charge-transfer processes of oxygen on the cathode and hydrogen on the anode. Plots of the R_{ohm}, R_p, and R_{tot} values vs. temperature are shown in Fig. 14(b). The values of R_p, R_{ohm}, and R_{tot} are seen to decrease with increasing temperature. The values of R_p are 0.593, 0.327, and 0.284 Ω cm^2 at 750, 800, and 850 °C, respectively. R_{tot} of the cell is mainly controlled by R_p; for example, 59.7% at 850 °C. Therefore, reducing R_p is critical for reducing R_{tot} to improve the cell performance.

The electrochemical stability of the Sr$_2$FeMoO$_{6-\delta}$ anode in H$_2$ was tested. Fig. 15 shows the cell P_{max} and the current density as functions of time at 850 °C in dry H$_2$. A total testing period of 20 h was used for the single cell with Sr$_2$FeMoO$_{6-\delta}$ as the anode. Power loss was calculated according to ($P_{max,0} - P_{max,20})/P_{max,0} \times 100\%$. Power loss in H$_2$ was 2.7% over a 20 h period, which indicates that Sr$_2$FeMoO$_{6-\delta}$ is a relatively stable anode material.
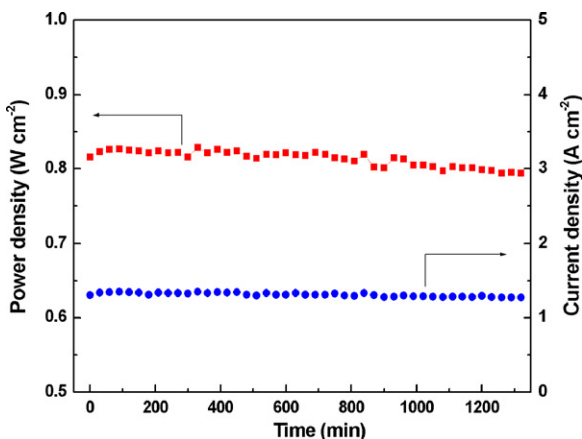
To assess the electrochemical performance of the Sr$_2$FeMoO$_{6-\delta}$ anode in a complex hydrocarbon fuel, a single cell with Sr$_2$FeMoO$_{6-\delta}$ as the anode was tested in humidified commercial city gas containing H$_2$S (3% H$_2$O). The commercial city gas composition is shown in Table 3 (from the commercial city gas supply system in Changchun). Fig. 16 shows the power density and cell voltage as functions of current density at different temperatures for a single cell with an Sr$_2$FeMoO$_{6-\delta}$ anode in the city gas containing H$_2$S (3% H$_2$O). The cell P_{max} reached 735, 476, and 183 mW cm^{-2} at 850, 800, and 750 °C, respectively. The cell P_{max} in the humidified city gas containing H$_2$S is obviously lower than that in H$_2$ due to the complex gas composition. Fig. 17 shows the cell P_{max} and the current density as functions of time at 800 °C in the humidi-
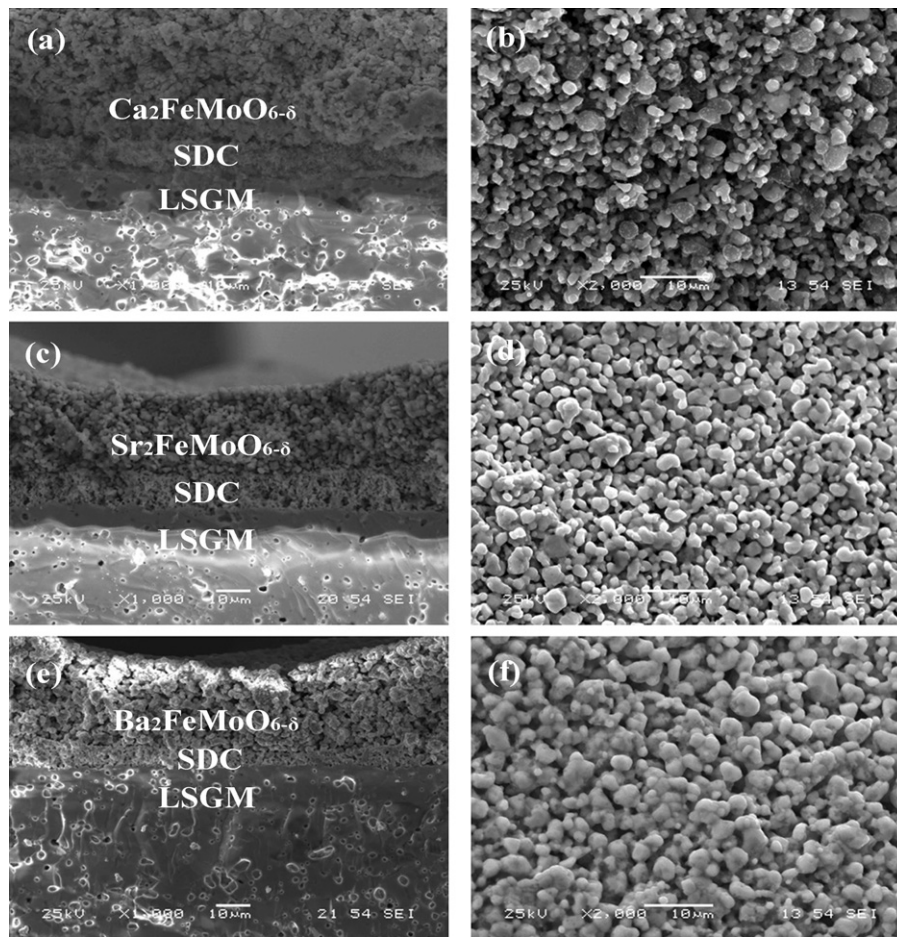
Fig. 13. SEM micrographs of the cell after testing: cross-section between $A_2FeMoO_{6-\delta}$ anode and LSGM electrolyte for (a) $Ca_2FeMoO_{6-\delta}$, (c) $Sr_2FeMoO_{6-\delta}$, and (e) $Ba_2FeMoO_{6-\delta}$; surface of $A_2FeMoO_{6-\delta}$ anodes for (b) $Ca_2FeMoO_{6-\delta}$, (d) $Sr_2FeMoO_{6-\delta}$, and (f) $Ba_2FeMoO_{6-\delta}$.

fied city gas containing H_2S (3% H_2O). During the first 200 min, the cell P_{max} decreases significantly from 476 to 436 mW cm^{-2}. However, thereafter it remains steady throughout the rest of the test, indicating excellent electrochemical stability. The initial decrease in the cell P_{max} may be associated with the establishment of full equilibrium of the system when the fuel is switched from H_2 to city gas. The cell P_{max} displayed a slight fluctuation in city gas. This small fluctuation may be partly attributed to the unstable city gas flow, arising from the direct utilization of city gas in the SOFC from a commercial city gas pipe. Similar fluctuation phenomena were

also observed for SOFCs using coal syngas and coal gas containing arsine as fuels [52,53]. No carbon deposition was observed on the anode surfaces during long electrochemical tests at high temperatures (see Fig. 13(d)), suggesting that $Sr_2FeMoO_{6-\delta}$ tolerates well both carbon and sulfur from commercial city gas containing H_2S. Thus, it is a good SOFC anode candidate for a variety of fuels.

Fig. 15. Electrochemcial stability of a single-cell with $Sr_2FeMoO_{6-\delta}$ anode at 850 °C in H_2.
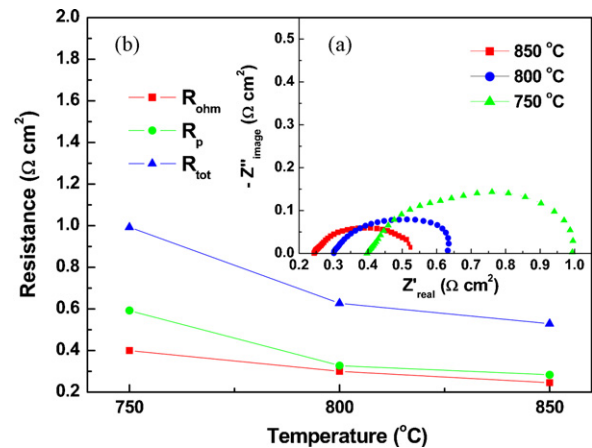

Fig. 14. (a) Impedance spectra of the single-cell with $Sr_2FeMoO_{6-\delta}$ anode measured at different temperatures under open-circuit conduction and (b) the interfacial polarization resistances (R_p), ohmic resistances (R_{ohm}), and total cell resistances (R_{tot}) determined from the impedance spectra as functions of temperatures.

Table 3
Components and contents of the commercial city gas and concentration of impurity gases (taken from Changchun City Gas Co., Ltd.).

Components	Percentage (%)	Concentration (ppm)
Methane	22.1	–
Hydrogen	59.6	–
Nitrogen	3.4	–
Carbon dioxide	2.3	–
Carbon monoxide	9.3	–
Oxygen	1	–
High hydrocarbon	2.3	–
Sulfureted hydrogen	–	4.92
Ammonia	–	11.87
Naphthaline	–	4.6
Coal tar	–	0.015
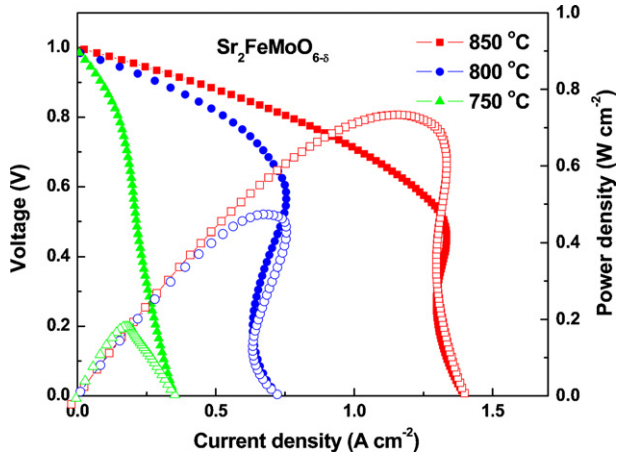
Fig. 16. Power density and cell voltage as functions of current density for a single-cell with $Sr_2FeMoO_{6-\delta}$ anode measured at different temperatures in commercial city gas containing H_2S (3% H_2O).
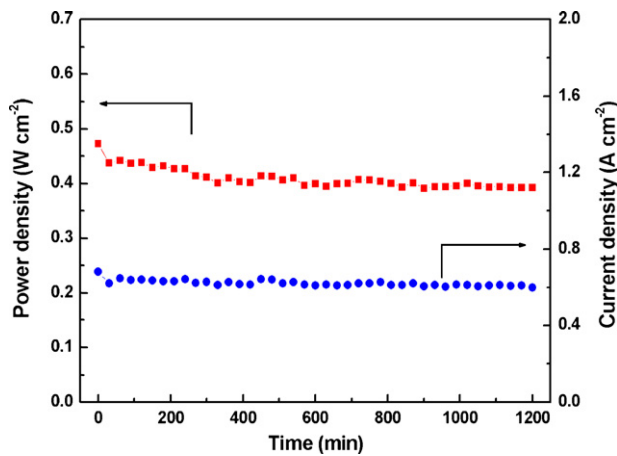
Fig. 17. Electrochemical stability of a single-cell with $Sr_2FeMoO_{6-\delta}$ anode at 800 °C in commercial city gas containing H_2S (3% H_2O).

4. Conclusions

Double-perovskites of the type $A_2FeMoO_{6-\delta}$ have been prepared by solid-state reactions and assessed as potential anode materials for use in SOFCs. The $A_2FeMoO_{6-\delta}$ compounds adopt monoclinic, tetragonal, and cubic structures for A = Ca, Sr, and Ba, respectively, at room temperature. Fe^{2+}–Mo^{6+} and Fe^{3+}–Mo^{5+} configurations co-exist in $A_2FeMoO_{6-\delta}$. The degeneracy and hybridization of the Fe^{2+}–Mo^{6+} and Fe^{3+}–Mo^{5+} states leads to the formation of a narrow band, which is responsible for the metallic conduction behavior

of these oxides. Regional semiconducting behavior observed for $Sr_2FeMoO_{6-\delta}$ and $Ba_2FeMoO_{6-\delta}$ may be related to a weak Anderson localization, i.e., the systems displayed disorder-induced localization of the charge carriers, thus resulting in a decrease in the electrical resistivity with increasing temperature. The large difference in the magnitudes of their electrical resistivities resulted from different degrees of degeneracy and hybridization between the Fe^{2+}–Mo^{6+} and Fe^{3+}–Mo^{5+} configurations. Whereas $Ca_2FeMoO_{6-\delta}$ proved to be unstable, $Sr_2FeMoO_{6-\delta}$ and $Ba_2FeMoO_{6-\delta}$ displayed excellent stabilities up to 1200 °C in a nitrogen atmosphere, and $Sr_2FeMoO_{6-\delta}$ showed the highest oxygen vacancy concentration. $Sr_2FeMoO_{6-\delta}$ and $Ba_2FeMoO_{6-\delta}$ displayed good thermal compatibility with LSGM electrolyte. The electrochemical performances of the $A_2FeMoO_{6-\delta}$ anodes in H_2 increased in the order: $Ca_2FeMoO_{6-\delta} < Ba_2FeMoO_{6-\delta} < Sr_2FeMoO_{6-\delta}$. The poor cell performance of the $Ca_2FeMoO_{6-\delta}$ anode was due to its decomposition at high temperatures and the low oxygen vacancy concentration. $Sr_2FeMoO_{6-\delta}$ exhibited a particularly favorable combination of high electrical conductivity, good thermal stability and thermal compatibility, and excellent electrochemical performance, and therefore can be recommended as a candidate anode material for use in SOFCs.

Acknowledgements

References

[1] E.P. Murray, T. Tsai, S.A. Barnett, Nature 400 (1999) 649–651.
[2] A. Atkinson, S. Barnett, R.J. Gorte, J.T.S. Irvine, A.J. McEvoy, M. Mogensen, S.C. Singhal, J. Vohs, Nat. Mater. 3 (2004) 17–27.
[3] J.B. Goodenough, Y.H. Huang, J. Power Sources 173 (2007) 1–10.
[4] S. Tao, J.T.S. Irvine, Nat. Mater. 2 (2003) 320–323.
[5] W. Zhu, S. Deevi, Mater. Sci. Eng. A 362 (2003) 228–239.
[6] S.P. Jiang, S.H. Chan, J. Mater. Sci. 39 (2004) 4405–4439.
[7] S. McIntosh, R.J. Gorte, Chem. Rev. 104 (2004) 4845–4865.
[8] S.W. Tao, J.T.S. Irvine, Chem. Rec. 4 (2004) 83–95.
[9] A. Lashtabeg, S.J. Skinner, J. Mater. Chem. 16 (2006) 3161–3170.
[10] C. Sun, U. Stimming, J. Power Sources 171 (2007) 247–260.
[11] E.V. Tsipis, V.V. Kharton, J. Solid State Electrochem. 12 (2008) 1367–1391.
[12] S. Zha, P. Tsang, Z. Cheng, M. Liu, J. Solid State Chem. 178 (2005) 1844–1850.
[13] Y.H. Huang, R.I. Dass, Z.L. Xing, J.B. Goodenough, Science 312 (2006) 254–257.
[14] Y.H. Huang, R.I. Dass, J.C. Denyszyn, J.B. Goodenough, J. Electrochem. Soc. 153 (2006) A1266–A1272.
[15] D. Marrero-Lopez, J. Pena-Martinez, J.C. Ruiz-Morales, D. Perez-Coll, M.A.G. Aranda, P. Nunez, Mater. Res. Bull. 43 (2008) 2441–2450.
[16] C. Bernuy-Lopez, M. Allix, C.A. Bridges, J.B. Claridge, M.J. Rosseinsky, Chem. Mater. 19 (2007) 1035–1043.
[17] Y.H. Huang, G. Liang, M. Croft, M. Lehtimaki, M. Karppinen, J.B. Goodenough, Chem. Mater. 21 (2009) 2319–2326.
[18] Y. Ji, Y.H. Huang, J.R. Ying, J.B. Goodenough, Electrochem. Commun. 9 (2007) 1881–1885.
[19] T. Wei, Y. Ji, X.W. Meng, Y.L. Zhang, Electrochem. Commun. 10 (2008) 1369–1372.
[20] T. Nakamura, K. Kunihara, Y. Hirose, Mater. Res. Bull. 16 (1981) 321–326.
[21] H. Falcón, J.A. Barbero, G. Araujo, M.T. Casais, M.J. Martínez-Lope, J.A. Alonso, J.L.G. Fierro, Appl. Catal. B-Environ. 53 (2004) 37–45.
[22] N. Yamazoe, Y. Teraoka, Catal. Today 8 (1990) 175–199.
[23] Q.J. Zhou, T.M. He, Y. Ji, J. Power Sources 185 (2008) 754–758.
[24] L.G. Cong, T.M. He, Y. Ji, P.F. Guan, Y.L. Huang, W.H. Su, J. Alloys Compd. 348 (2003) 325–331.
[25] Y. Shen, M.N. Liu, T.M. He, S.P. Jiang, J. Am. Ceram. Soc. 92 (2009) 2259–2264.
[26] J.B. Philipp, P. Majewski, L. Alff, A. Erb, R. Gross, T. Graf, M.S. Brandt, J. Simon, T. Whather, W. Mader, D. Topwal, D.D. Sarma, Phys. Rev. B 68 (2003) 144431–144443.
[27] L.H. Son, N.X. Phuc, P.V. Phuc, N.M. Hong, L.V. Hong, J. Raman Spectrosc. 32 (2001) 817–820.
[28] T. Zhang, W.R. Brandford, H.J. Trodahl, A. Sarma, J. Rager, J.L. MacManus-Driscoli, F. Cohen, J. Raman Spectrosc. 35 (2004) 1081–1085.
[29] S.P.S. Porto, J.F. Scott, Phys. Rev. 157 (1967) 716–719.
[30] N.A. Merino, B.P. Barbero, C. Cellier, J.A. Gamboa, L.E. Cadús, Catal. Lett. 113 (2007) 130–140.
[31] J.L.G. Fierro, Catal. Today 8 (1990) 153–174.

[32] K. Tabata, S. Kohiki, J. Mater. Sci. Lett. 6 (1987) 1030–1032.
[33] S. Bartkowski, M. Neumann, E.Z. Kurmaev, V.V. Federenko, S.N. Shamin, V.M. Cherkashenko, S.N. Memnonov, A. Winiarski, D.C. Rubie, Phys. Rev. B 56 (1997) 10656–10667.
[34] C. Cantalini, L. Lozzi, A. Passacantando, S. Santucci, IEEE Sens. J. 3 (2003) 171–179.
[35] K. Kuepper, I. Balasz, H. Hesse, A. Winiarski, K.C. Prince, M. Matteucci, D. Wett, R. Szargan, E. Burzo, M. Neumann, Phys. Status Solidi A 201 (2004) 3252–3256.
[36] M. Besse, V. Cros, A. Barthélémy, H. Jaffrès, J. Vogel, F. Petroff, A. Mirone, A. Tagliaferri, P. Bencok, P. Decorse, P. Berthet, Z. Szotek, W.M. Temmerman, S.S. Dhesi, N.B. Brookes, A. Rogalev, A. Fert, Europhys. Lett. 60 (2002) 608.
[37] Y. Yasukawa, J. Lindén, T.S. Chan, R.S. Liu, H. Yamauchi, M. Karppinen, J. Solid State Chem. 177 (2004) 2655–2662.
[38] P. Woodward, R.-D. Hoffmann, A.W. Sleight, J. Mater. Res. 9 (1994) 2118–2127.
[39] D. Niebieskikwiat, R.D. Sánchez, A. Caneiro, L. Morales, M. Vásquez-Mansilla, F. Rivadulla, L.E. Hueso, Phys. Rev. B 62 (2000) 3340–3345.
[40] A.W. Sleight, J.F. Weiher, J. Phys. Chem. Solids 33 (1972) 679–687.
[41] K.-I. Kobayashi, T. Kimura, H. Sawada, K. Terakura, Y. Tokura, Nature 395 (1998) 677–680.
[42] C. Zener, Phys. Rev. 82 (1951) 403–409.
[43] M. Itoh, I. Ohta, Y. Inaguma, Mater. Sci. Eng. B 41 (1996) 55–58.
[44] R. Allub, B. Alascio, Phys. Rev. B 55 (1997) 14113–14116.
[45] Y. Matsuda, M. Karppinen, Y. Yamazaki, H. Yamauchi, J. Solid State Chem. 182 (2009) 1713–1716.
[46] D. Marrero-López, J. Peña-Martínez, J.C. Ruiz-Morales, M. Gabás, P. Núñez, M.A.G. Aranda, J.R. Ramos-Barrado, Solid State Ionics 180 (2010) 1672–1682.
[47] M.A. Peña, J.L.G. Fierro, Chem. Rev. 101 (2001) 1981–2017.
[48] G. Pacchioni, Chem. Phys. Chem. 4 (2003) 1041–1047.
[49] M. Mori, N.M. Sammes, Solid State Ionics 146 (2002) 301–312.
[50] S. Onuma, K. Yashiro, S. Miyoshi, A. Kaimai, H. Matsumoto, Y. Nigara, T. Kawada, J. Mizusaki, K. Kawamura, N. Sakai, H. Yokokawa, Solid State Ionics 174 (2004) 287–293.
[51] E.P. Murray, S.A. Barnett, Solid State Ionics 143 (2001) 265–273.
[52] J.E. Bao, G.N. Krishnan, P. Jayaweera, J. Perez-Mariano, A. Sanjurjo, J. Power Sources 193 (2009) 607–616.
[53] C.A. Coyle, O.A. Marina, E.C. Thomsen, D.J. Edwards, C.D. Cramer, G.W. Coffey, L.R. Pederson, J. Power Sources 193 (2009) 730–738.